Check for updates

ADVANCED ENERGY MATERIALS
www.advenergymat.de

Interface Welding via Thermal Pulse Sintering to Enable 4.6 V Solid-State Batteries

Xiangming Yao, Shiming Chen, Changhong Wang, Taowen Chen, Jiangxiao Li, Shida Xue, Zhikang Deng, Wenguang Zhao, Bowen Nan, Yiqian Zhao, Kai Yang, Yongli Song, Feng Pan, Luyi Yang, and Xueliang Sun**

NASICON-type $Li_{1.3}Al_{0.3}Ti_{1.7}(PO4)_3$ (LATP) is one of the most promising solid-state electrolytes (SSEs) to achieve high-energy-density solid-state batteries (SSBs) due to its high ionic conductivity, high-voltage stability, and low cost. However, its practical application is constrained by inadequate interfacial compatibility with cathode materials and significant incompatibility with lithium metal. In this work, a cost-effective interface welding approach is reported, utilizing an innovative thermal pulse sintering (TPS) to fabricate LATP-based solid-state batteries. Initially, the rapid thermal pulses enhance the ionic conductivity of LATP SSE by inducing selective growth of LATP nanowires, effectively occupying interparticle voids. Additionally, this process results in the formation of a dense layer (GCM) comprising graphene oxide, carbon nanotubes, and MXene with a controlled Li^+ transport pathway, facilitating lithium stripping and plating processes. Moreover, these thermal pulses facilitate the interfacial fusion between LATP and cathode materials, while avoiding undesired phase diffusion. As a result, SSBs with a $LiCoO_2$ cathode deliver favorable cycle stability at 4.6 V, marking significant progress. This facile interface welding strategy represents a substantial step toward high-energy-density SSB development.

1. Introduction

The pursuit of high-energy-density Li-ion batteries has become a major trend for future battery development, which requires the incorporation of high-energy-density cathode and anode materials.[1,2] However, such a combination faces a series of problems: on the one hand, high-voltage cathodes, such as lithium cobalt oxides ($LiCoO_2$), have poor interfacial stability toward traditional organic electrolyte solvents during high-voltage operations; on the other hand, as the "holy grail" of anode materials, Li metal suffers from dendritic Li formation and poor Coulombic efficiency.[3,4] Exhibiting high Li-ion conductivity, wide electrochemical windows, and the ability to inhibit dendrite growth, inorganic solid electrolyte (ISEs) is regarded as a promising substitution for liquid electrolytes to realize high-energy-density batteries.[5]

X. Yao, S. Chen, T. Chen, S. Xue, Z. Deng, W. Zhao, B. Nan, Y. Zhao, F. Pan, L. Yang
School of Advanced Materials
Peking University Shenzhen Graduate School
Shenzhen 518055, P. R. China
E-mail: yangly@pkusz.edu.cn

C. Wang, X. Sun
Eastern Institute for Advanced Study
Eastern Institute of Technology
Ningbo, Zhejiang 315200, P. R. China
E-mail: xsun@eng.uwo.ca

J. Li
National Synchrotron Radiation Laboratory
University of Science and Technology of China
Hefei 230029, P. R. China

K. Yang
Advanced Technology Institute
Department of Electrical and Electronic Engineering
University of Surrey
Guildford, Surrey GU2 7XH, UK

Y. Song
School of Energy and Power Engineering
Jiangsu University
Zhenjiang 212013, P. R. China

X. Sun
Department of Mechanical and Materials Engineering
University of Western Ontario
1151 Richmond Street, London, Ontario N6A 3K7, Canada

The ORCID identification number(s) for the author(s) of this article can be found under https://doi.org/10.1002/aenm.202303422

© 2023 The Authors. Advanced Energy Materials published by Wiley-VCH GmbH. This is an open access article under the terms of the Creative Commons Attribution-NonCommercial-NoDerivs License, which permits use and distribution in any medium, provided the original work is properly cited, the use is non-commercial and no modifications or adaptations are made.

DOI: 10.1002/aenm.202303422

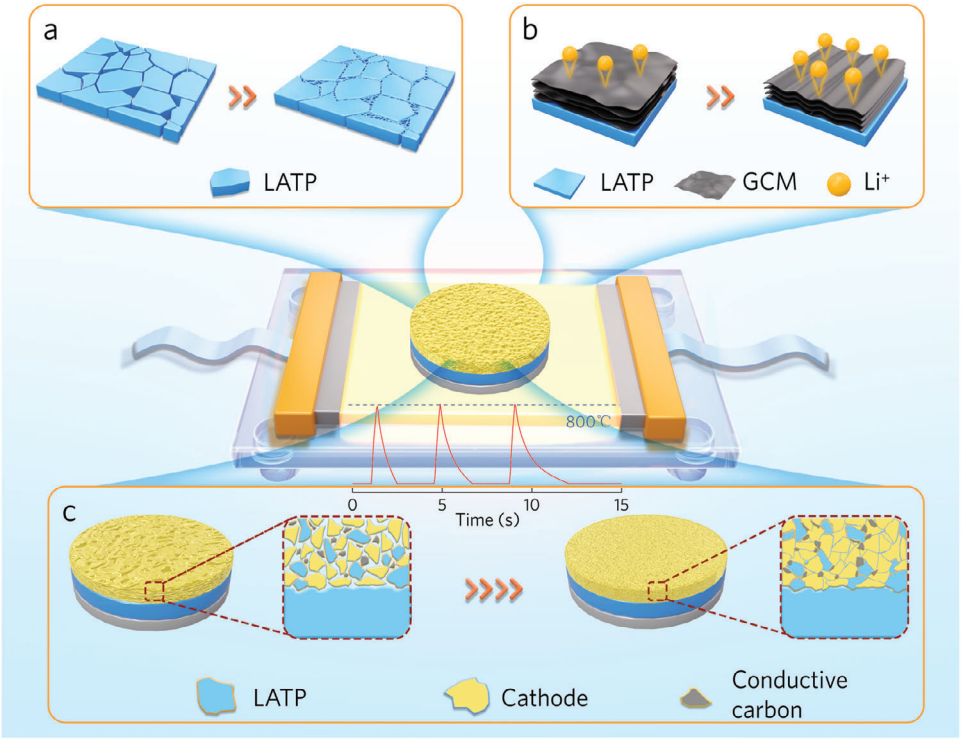

Scheme 1. Schematic illustration of TPS and its impact on the SSB: a) Ultrahigh heating rate enhances the densification of SSE via void filling. b) Morphology as well as Li^+ pathways in the GCM layer is regulated. c) Interfacial contact between active particles, acetylene black, and LATP particles is vastly improved.

Among various ISEs, NASICON-type $Li_{1+x}Al_xTi_{2-x}(PO_4)_3$ (LATP, x = 0.3–0.5) has been extensively investigated owing to its high ionic conductivity, high-voltage compatibility, relatively low sintering temperature and prominent stability for ambient operations.[6,7] Unfortunately, the poor contact between LATP and cathode materials and its continuous side reactions with Li anode have hindered the development of LATP-based all-solid-state batteries.[8,9] In order to mitigate the interfacial issues, approaches such as adding a small amount of catholyte or applying a polymeric buffer layer at the anode side are often adopted.[10,11] Nevertheless, the addition of organic components not only induces undesirable reactions at high voltages but also decreases the thermal stability of the battery.[12,13] Alternatively, integrated sintering methods of adding inorganic sintering additives to improve the interface contact have been widely studied.[14,15] However, side effects (e.g., phase diffusion and Li loss) introduced by long-term high-temperature treatment result in irreversible damage to both LATP and active materials, thus leading to performance decay.[16] Therefore, an effective and convenient interface welding strategy is highly desirable for addressing the above-mentioned interfacial issues of LATP-based SSBs.

In this work, a modified ultrafast high-temperature sintering (UHS) method—thermal pulse sintering (TPS)—is employed to achieve rapid (≈10 s) integrated sintering for high-voltage SSBs (**Scheme 1**). By dividing the continuous UHS into multiple (e.g., 3) thermal pulses, TPS aims to minimize undesirable interfacial side reactions. First, instead of interfacial melting, the thermal pulse treatment can significantly densify the SSE ceramic by inducing LATP nanowires (NWs) within the voids, which further interconnect and fill up the space, thus greatly improving ionic conductivity (Scheme 1a). Second, a novel graphene oxide-carbon nanotube-MXene (GCM) layer is fabricated on the anode side of LATP to prevent side reactions with Li. The thermal shock not only enables homogeneous and uniform layer morphology to better suppress Li dendrite, but also facilitates interfacial Li^+ pathways (Scheme 1b). Third, the thermal pulse welds the cathode tightly with the electrolyte within seconds without causing undesirable phase diffusions (Scheme 1c). Based on the above-mentioned multifaceted optimizations, the as-fabricated SSB enables high-voltage operation as high as 4.6 V.

2. Results and Discussion

2.1. Densification of LATP Through Void-Filling

First, the impact of various thermal treatments on the bulk conductivity of LATP is evaluated via electrochemical impedance spectroscopy (EIS, Figure S1, Supporting Information). Furnace sintering (FS) and TPS could improve the room-temperature ionic conductivity of pristine LATP from 1.57×10^{-4} S cm^{-1} to 5.35×10^{-4} S cm^{-1} and 8.20×10^{-4} S cm^{-1}, respectively (**Figure 1a**). Through measuring the relative densities of different LATP pellets (Figure 1b), it is shown that the TPS method results in a much higher relative density of 98.1% compared with pristine LATP (92.8%) and furnace-heated LATP (93.6%). It is intriguing that the TPS method achieves a much denser LATP pellet with a relatively low heating time than the FS method. To reveal the

© 2023 The Authors. Advanced Energy Materials published by Wiley-VCH GmbH

16146840, 2024, 10, Downloaded from https://advanced.onlinelibrary.wiley.com/doi/10.1002/aenm.202303422 by University Town Of Shenzhen, Wiley Online Library on [19/11/2025]. See the Terms and Conditions (https://onlinelibrary.wiley.com/terms-and-conditions) on Wiley Online Library for rules of use; OA articles are governed by the applicable Creative Commons License

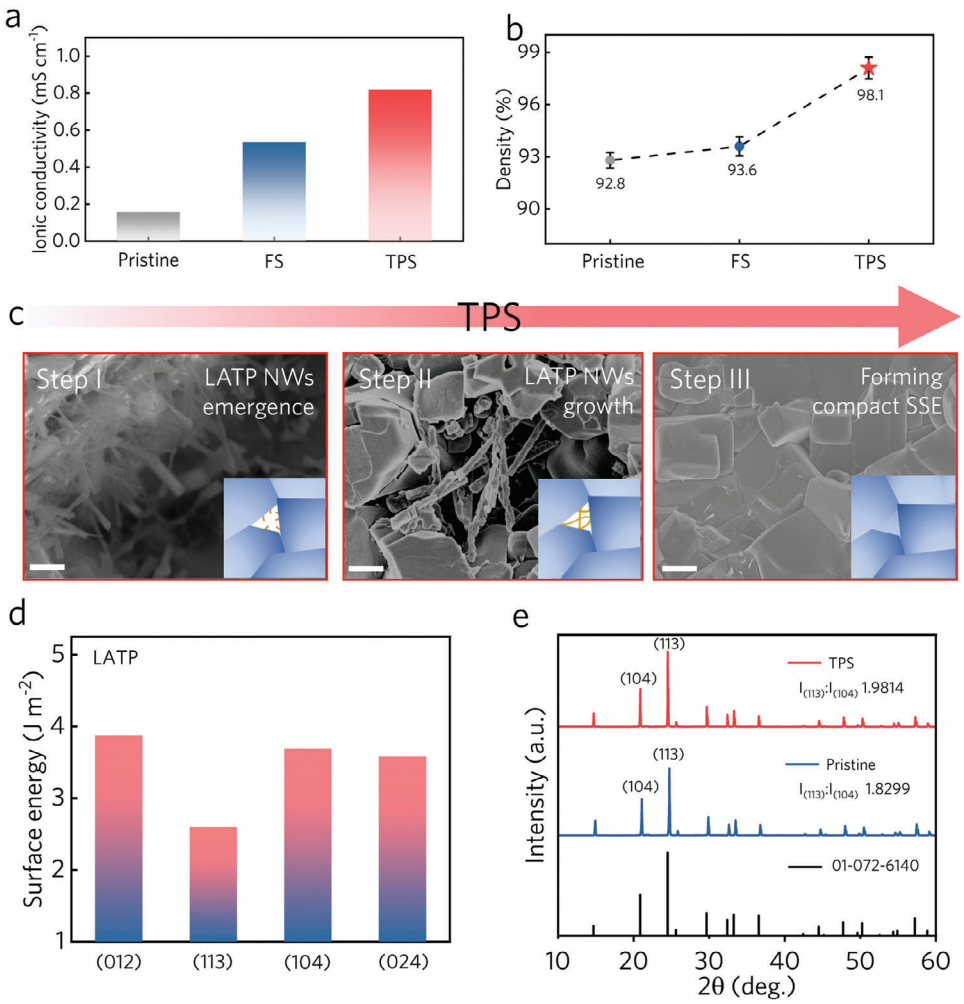

Figure 1. Ionic conductivity a) and relative densities b) of LATP pellets prepared via different sintering methods. c) SEM images and the corresponding schematic diagrams (insets) of LATP densification through void-filling by TPS. Scale bars = 2 µm. d) Calculated surface energy of 4 main orientations in LATP. e) X-ray diffusion (XRD) patterns of LATP pellet prepared via different sintering methods.

underlying causes, the structural evolution of thermal pulse-heated LATP pellets is examined through a scanning electron microscope (SEM, Figure 1c). Cross-sectional SEM images of LATP pellets under various thermal treatment states show that at the beginning, LATP NWs are formed from the particle, which can be confirmed by the elemental mapping images (Figure S2, Supporting Information). With further heating, these NWs start to intertwine and granulate within the pellets (inset, Figure 1c). Eventually, a densified LATP pellet can be obtained. In comparison, such morphology evolution cannot be observed in a furnace-heated LATP pellets (Figure S3, Supporting Information). Combining the above results, two promoting mechanisms for the ionic conductivity of LATP can be proposed: 1) furnace heating could achieve better contact between LATP particles through welding the existing interfaces, hence an improved ionic conductivity is obtained without significant density variation; 2) the thermal pulse heating not only facilitates better interfacial contact but also greatly densifies LATP pellets through void filling, where NWs continuously form and grow until they filled up the entire pore space, resulting in extra Li^+ conduction pathways.

To investigate the growing mechanism of LATP NWs, experimental and theoretical investigations have been carried out. According to different orientation surface energies (Figure 1d), the (113) crystal plane of LATP exhibits the lowest surface energy (2.6 J m^{-2}) than other facets,[17,18] hence the thermodynamically most stable facet. Therefore, LATP will preferentially grow along this plane during the transient melting-recrystallization process under a rapid thermal pulse, resulting in the formation of fiber-like 1D LATP.[19] This speculation is confirmed by the X-ray diffraction (XRD) results, where the intensity of the relative (113) crystal plane $I_{(113)}$ is improved after the thermal shock (Figure 1e), implying that the LATP NWs originate from its oriented growth along (113) plane.

2.2. Li^+ Fast-Tracks Facilitated by a Compact Buffer Layer

To avoid direct contact between LATP and Li metal anode, the surface of the thermal pulse sintered LATP pellet is modified with a layer of GCM. However, the GCM layer without TPS

© 2023 The Authors. Advanced Energy Materials published by Wiley-VCH GmbH

16146840, 2024, 10, Downloaded from https://advanced.onlinelibrary.wiley.com/doi/10.1002/aenm.202303422 by University Town Of Shenzhen, Wiley Online Library on [19/11/2025]. See the Terms and Conditions (https://onlinelibrary.wiley.com/terms-and-conditions) on Wiley Online Library for rules of use; OA articles are governed by the applicable Creative Commons License

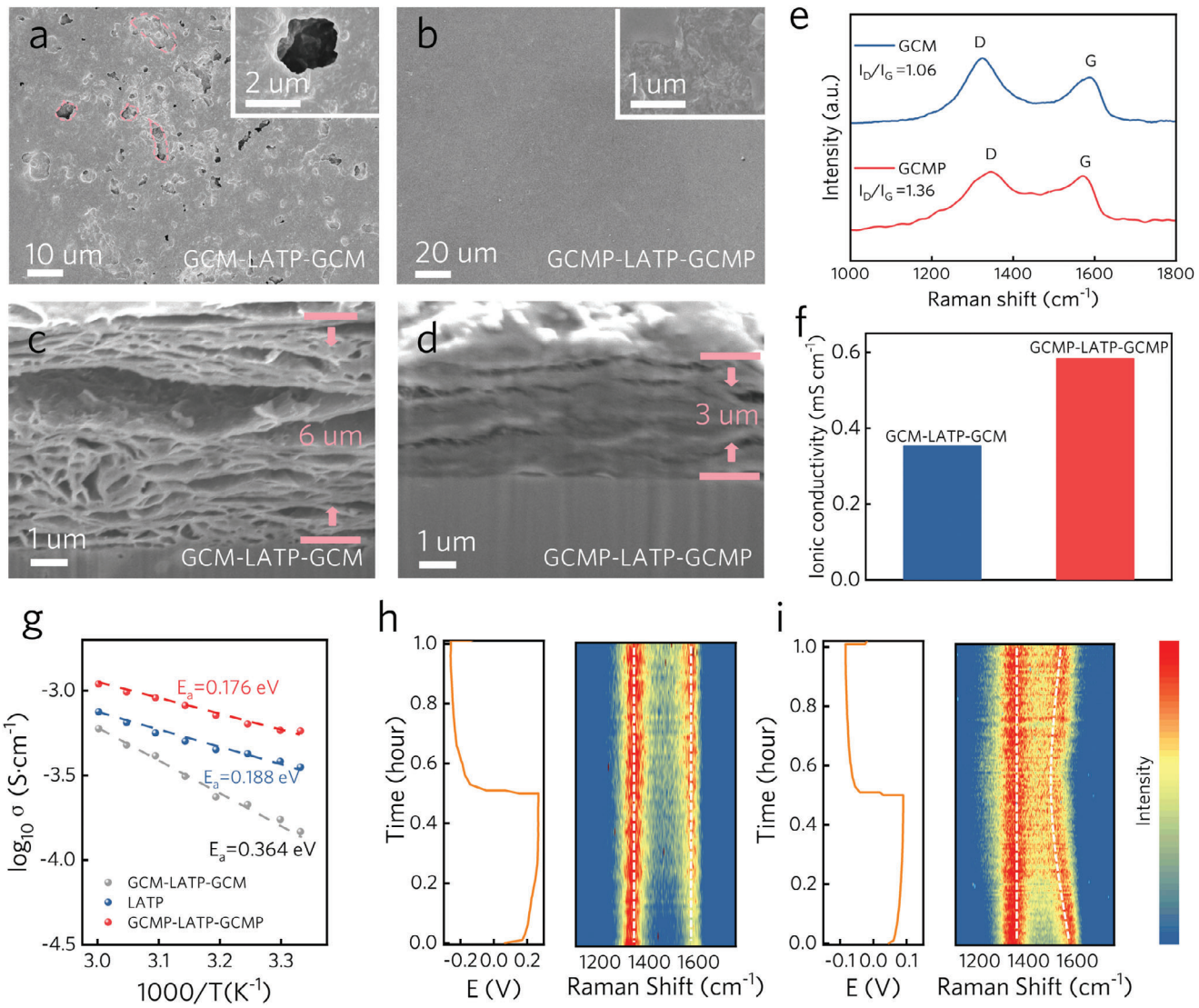

Figure 2. Top-viewed a) and cross-section c) SEM images of GCM-LATP. b) Top-viewed and cross-section (d) SEM images of GCMP-LATP. e) Raman spectra of GCM and GCMP layer. f) Ionic conductivity of LATP, GCM-LATP-GCM, and GCMP-LATP-GCMP. g) Arrhenius plots of LATP, GCM-LATP-GCM and GCMP-LATP-GCMP. h,i) In situ Raman spectra of Li/GCM-LATP-GCM/Li and Li/GCMP-LATP-GCMP/Li.

treatment not only exhibits uneven surfaces with many pinholes, but also shows loose cross-sectional structure (**Figure** 2a–c), which is unfavorable for Li^+ conduction through the GCM layer. In comparison, the thermal pulse-treated GCM layer (denoted as GCMP) shows a much smoother surface and compact bulk structure (Figure 2b–d). It is worth noting that the GCM layer breaks apart after furnace sintering (Figure S4, Supporting Information), which will not be further discussed. The componential evolution of GCM during thermal pulse heating is investigated via Raman spectroscopy (Figure 2e). After the thermal treatment, the peak intensity ratio of the D (≈1350 cm^{-1}) and G (≈1590 cm^{-1}) bands ($I_{(D)}/I_{(G)}$) decreased from 1.36 to 1.06, indicating a higher degree of graphitization, which might be beneficial for the process of Li^+ migration.

EIS of Au||GCM-LATP-GCM||Au and Au||GCMP-LATP-GCMP||Au symmetrical cells at 25 °C were compared to investigate the ionic conductivity of the coating layers (Figure 2f; Figure S5, Supporting Information). The ionic conductivity of GCM-LATP-GCM is measured to be 3.53×10^{-4} S cm^{-1}, significantly lower than the LATP pellet due to the sluggish LATP-GCM interfacial charge transfer. By contrast, thanks to the well-contacted interface and the enhanced ion conduction in GCMP, GCMP-LATP-GCMP exhibits a room-temperature ionic conductivity as high as 5.83×10^{-4} S cm^{-1}, indicating the promoted Li^+ conduction in the GCMP layer. In addition, GCMP-LATP-GCMP also presents a lower activation energy than GCM-LATP-GCM (Figure 2g), suggesting a lowered Li^+ transport barrier. The speculation is confirmed by the ion conductivity results of GCM and GCMP layers (Figure S6, Supporting Information), where the ion conductivity of the GCMP layer (2.6×10^{-4} S cm^{-1}) surpasses that of the original GCM layer (2.2×10^{-7} S cm^{-1}) by three orders of magnitude. Moreover,

© 2023 The Authors. Advanced Energy Materials published by Wiley-VCH GmbH

16146840, 2024, 10, Downloaded from https://advanced.onlinelibrary.wiley.com/doi/10.1002/aenm.202303422 by University Town Of Shenzhen, Wiley Online Library on [19/11/2025]. See the Terms and Conditions (https://onlinelibrary.wiley.com/terms-and-conditions) on Wiley Online Library for rules of use; OA articles are governed by the applicable Creative Commons License

Li symmetric cells employing the GCMP-LATP-GCMP electrolyte also exhibit a lower impedance (Figure S7, Supporting Information). In order to study the Li^+ migration behaviors in GCMP, in situ Raman analysis was conducted in Li-symmetric cells (Figure 2h,i). All lithium anodes were moistened with 2 µL electrolyte (see more details in Supporting Information). It is shown that during Li plating, the G band of GCMP blueshifted, indicating Li^+ insertion into the graphite structure; upon Li stripping, the G band of GCMP shifted back, suggesting Li de-intercalation from the graphite structure. In comparison, the GCM layer shows no such peak change.[20] This result verifies that the graphitized GCMP structure facilitates a large number of Li^+ transport and storage channels, which potentially enables reversible Li redox. Furthermore, 2D mapping of Raman analysis (Figure S8, Supporting Information) illustrates that after 30 min of charging treatment, the distance between D peaks and G peaks in the 100 × 100 µm range of the surface area of the GCMP layer is significantly reduced, suggesting that its lithium conduction pathway is uniformly distributed in a large area.

2.3. Thermal-Induced Interface Welding for Cathodes

Compared with the sintering processes of anode or bulk SSE, the cathode sintering for high-performance SSEs is more complicated: on the one hand, all interfaces should be well connected with minimum voids; on the other hand, over-sintering leads to phase diffusion between active material and SSE particles. Hence, balancing the degree of sintering for cathode composite electrodes has a vital impact on the delivery of cell capacities.[14] To verify the universality of this method for cathode sintering, nano-sized $LiFePO_4$ (LFP) and micro-sized $LiCoO_2$ (LCO) active materials (SEM images shown in Figure S9, Supporting Information) have been used. The cross-sectional images (**Figure 3**a–c) and the corresponding EDS maps (Figure S10, Supporting Information) of untreated cathode/SSE interfaces indicate poor physical contact between the cathode and SSE, with large gaps as wide as 2–5 µm. After TPS and FS treatment, cathodes are in better contact with SSEs, enabling fast ionic conduction across the interface (Figure 3c,d; Figure S10, Supporting Information). Tape tests showed that before sintering, the cathode composite could be peeled off easily from the surface of the LATP, indicating insufficient interfacial contact; whereas the sintered cathode composites were tightly bonded to the LATP surface without being peeled off, confirming the improved interface adhesion between cathode and LATP (Figure S11, Supporting Information).

In addition to the interfacial contact between the composite cathode and SSE pellet, the compactness within the composite cathode is equally essential. 3D reconstruction by focused-ion beam (FIB) was previously demonstrated to be effective in differentiating different components and voids in composite electrodes.[21] Herein, the impact of sintering methods on the compactness of cathodes was further investigated through 3D FIB (Figure 3e). Quantitative analysis shows that within a selected region, the density of both LFP and LCO cathodes increased after FS and TPS by exhibiting much smaller contents of voids. The improved compactness implies well-welded solid–solid interfaces, which create a continuous Li^+ and electron conduction network in the electrode.[22] Furthermore, the TPS method is able to fill the gaps and voids better than FS by reducing the voids to merely 1.8%. To elucidate the origin of the phenomenon during the TPS process, finite element simulations demonstrated that the contact point between the conductive materials will generate more joule heat due to higher resistance, thus forming a local thermal field to accelerate the welding of LATP and cathode active materials (Figure S12, Supporting Information). These results also agree with top-view SEM images of various cathodes (Figures S13 and S14, Supporting Information), where cathodes treated with thermal pulse exhibit the highest compactness. In contrast, the untreated cathodes exhibit loose structures.

To determine interfacial side reactions induced by thermal treatment, XRD patterns of cathode mixtures (i.e., active materials, LATP, and acetylene black) were examined (**Figure 4**a; Figure S15, Supporting Information). After TPS, no phase transition or byproduct phases can be indexed in both LCO and LFP cathodes, suggesting interfacial side reactions were inhibited due to the limited heating time. However, both LCO and LFP cathodes exhibit peaks arising from byproducts after FS, which is mainly due to the side reaction between active materials and LATP during prolonged thermal treatment. For the LFP cathode, the main side product is the Fe-deficient $Li_3Fe_2(PO_4)_3$ phase, which might be attributed to the diffusion of Fe into LATP, forming Fe-doped LATP.[15] To verify this speculation, element mapping of sintered LFP/LATP interfaces has been carried out. As expected, severe Fe diffusion into LATP occurred after FS treatment, forming Fe-doped LATP (Figure 4b). In comparison, after TPS treatment, Fe is concentrated within the LFP powder, forming a distinct interface with LATP (Figure 4c). Cryo-transmission electron microscopy (cryo-TEM) observation was further carried out to study the interfacial crystalline structures between LATP and LFP (Figure S16, Supporting Information) after thermal pulse sintering. The interplanar spacing corresponding to the (020) lattice planes of LFP and the crystal plane spacing of the (104) crystal plane of LATP can be well defined from the cryo-TEM image.[15] The firmly welded grain boundaries of LATP and LFP are beneficial to Li-ion transport. The emerging Ti^{3+} (458.0, 464.1 eV) signal in Ti 2p XPS spectra[7,10] (Figure S17, Supporting Information) as well as the reduced relative Raman peak intensity of P–O symmetric stretching vibration (952 cm^{-1}, $\nu 1$)[23,24] (Figure S18, Supporting Information) have also confirmed the proposed side reaction of Fe diffusion into LATP has occurred the furnace sintered LFP cathode.[15] Furthermore, in situ Raman spectra show that the characteristic peak of LATP at 1034 cm^{-1} also intensified during discharging (Figure S19, Supporting Information), indicating the Fe-doped LATP is involved in the electrochemical cycling.

As for LCO composite cathodes, XRD patterns (Figure 4d) showed that the crystalline structure of cathode prepared through TPS remained stable, while FS results in large amounts of byproducts, including Co_3O_4, CoO_2, and Li_3PO_4, which agrees with the disappeared Co–O stretching vibration (590 cm^{-1}, A_{1g}) of LCO[24] and the emerging Co_3O_4 peaks (≈684 cm^{-1})[25] in the Raman spectra (Figure S20, Supporting Information). EDS mappings of the LCO/LATP interface sintered by the furnace exhibit even more severe interdiffusion, indicating serious side reactions have occurred (Figure 4e), whereas LCO/LATP shows a well-defined interface without apparent Co or Ti diffusion (Figure 4f).

© 2023 The Authors. Advanced Energy Materials published by Wiley-VCH GmbH

16146840, 2024, 10, Downloaded from https://advanced.onlinelibrary.wiley.com/doi/10.1002/aenm.202303422 by University Town Of Shenzhen, Wiley Online Library on [19/11/2025]. See the Terms and Conditions (https://onlinelibrary.wiley.com/terms-and-conditions) on Wiley Online Library for rules of use; OA articles are governed by the applicable Creative Commons License

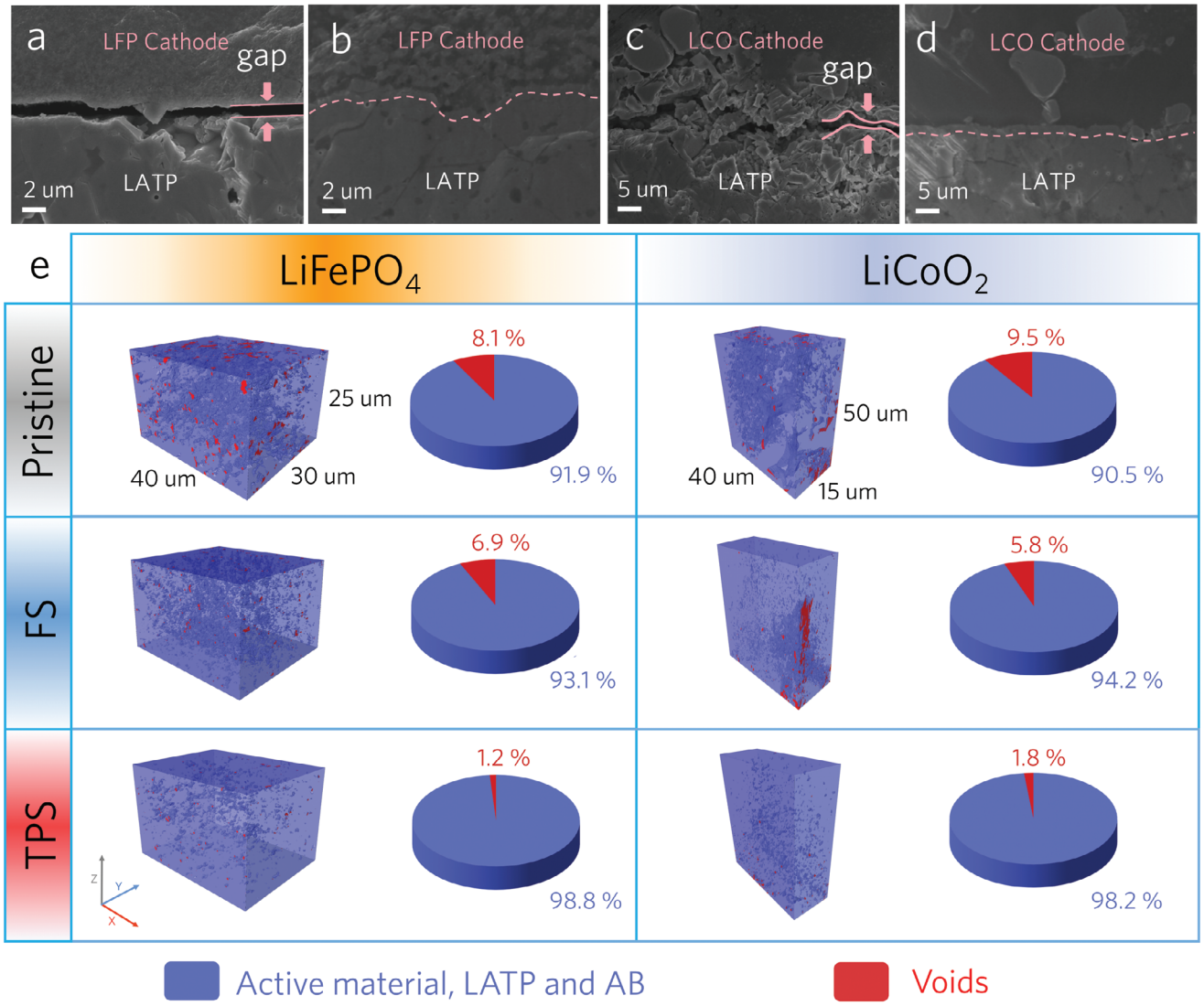

Figure 3. Cross-section SEM images of $LiFePO_4$ cathode/SSE interface before a) and after b) TPS process. Cross-section SEM images of $LiCoO_2$ cathode/SSE interface before c) and after d) TPS process. e) 3D image reconstruction and the corresponding quantitative analysis of different components in cathodes before and after FS, TPS process.

Co L-edge soft XAS results (Figure S21, Supporting Information) also exhibit a significant increase of Co^{2+} in the LCO cathode treated by FS, implying the occurrence of side effects during long-term heat treatment.[26] Consequently, the Li||GCMP-LATP||LCO full cell prepared through FS barely releases any capacity, accompanied by the surge in charge transfer impedance (Figures S22 and S23, Supporting Information). Such severe phase changes for LCO cathode could be attributed to the lower thermal stability of layered oxides compared with polyanion oxides,[27] leading to violent reaction with LATP[14]:

$$12Li_{1.5}Al_{0.5}Ti_{1.5}(PO_4)_3 + 36LiCoO_2 \rightarrow 12Li_3PO_4 + 6AlPO_4 + 18LiTiPO_5 + 9Co_3O_4 + 9CoO_2 \quad (1)$$

$$\Delta G = -16.13\ \text{eV} \quad (2)$$

2.4. Electrochemical Performance of All-Solid-State Batteries

Continuous Li plating/stripping tests using different electrolytes in symmetric cells were performed to evaluate their electrochemical stability with Li metal anodes (Figure 5a; Figure S24a, Supporting Information). Under a constant current density of 0.2 mA cm^{-2}, the overpotential of Li||LATP||Li cell reaches over 500 mV after 50 h of cycling. According to the post-mortem XPS results (Figure S25, Supporting information), this is mainly due to the continuous chemical reduction of Ti^{4+} by Li, forming a high-impedance interfacial layer. In contrast, both GCM and GCMP layers could inhibit the above-mentioned side reactions by cutting off the direct electronic transfer, resulting in much lower overpotentials in symmetric cells. Notably, the GCMP-coated LATP achieves a much lower initial overpotential (≈100 mV) than GCM-coated LATP (≈260 mV), which can be attributed to the promoted interfacial Li^+ transfer. Moreover, the overpotential of

© 2023 The Authors. Advanced Energy Materials published by Wiley-VCH GmbH

16146840, 2024, 10, Downloaded from https://advanced.onlinelibrary.wiley.com/doi/10.1002/aenm.202303422 by University Town Of Shenzhen, Wiley Online Library on [19/11/2025]. See the Terms and Conditions (https://onlinelibrary.wiley.com/terms-and-conditions) on Wiley Online Library for rules of use; OA articles are governed by the applicable Creative Commons License

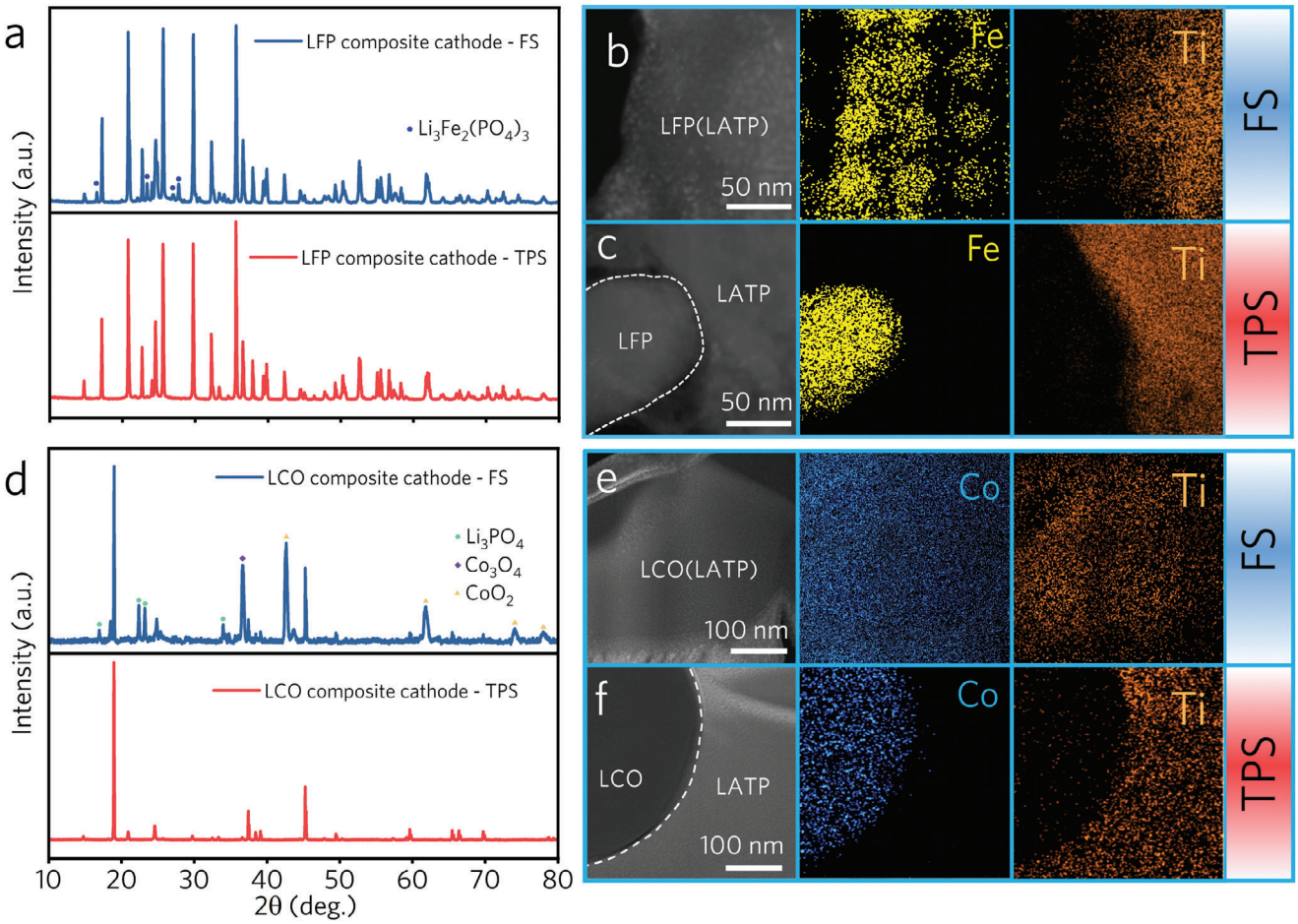

Figure 4. a) XRD patterns of LFP cathode composites after treatment of different sintering methods. TEM images of LFP/LATP particles after b) FS and c) TPS with corresponding elemental mapping of Fe and Ti. d) XRD patterns of LCO cathode composites after treatment of different sintering methods. TEM images of LCO/LATP particles after e) FS and f) TPS with corresponding elemental mapping of Co and Ti.

Li||GCM-LATP-GCM||Li increased gradually during cycling, suggesting side reactions between Li and LATP still occurred despite the protection of GCM. This is confirmed by the Ti-L2 and Ti-L3 soft XAS results (Figure S26, Supporting Information) of LATP pellets after cycling, where the increased I_{t2g}/I_{eg} ratio measured on GCM-LATP-GCM indicates the generation of Ti^{3+}.[26] Through examining the surface morphologies of cycled LATP, Li dendrites are found to be embedded into both the unprotected LATP (Figure S27, Supporting Information) and GCM-coated LATP (Figure 5b), resulting in obvious cracks. In sharp contrast, no Li penetration was found on LATPs protected by the GCMP layer, showcasing its capability of preventing Li dendrite growth. It is reasonable to speculate that compared with the pinhole-free structure of GCMP, the defects existing in GCM could induce Li dendrite growth, resulting in its direct contact with LATP. Surface morphologies of cycled Li anodes (Figure S28, Supporting Information) also support this conclusion: compared with GCM, GCMP could effectively regulate the Li plating/stripping, maintaining a homogeneous Li anode surface during prolonged cycling.

The rate capability of the modified LATP-Li interface was tested by applying an increasing current density in Li-symmetric cells. The cell using LATP failed at the current density of 0.8 mA cm^{-2} due to short-circuit (Figure S24b, Supporting Information). By comparison, LATP modified by GCM and GCMP delivered much-improved limiting current densities of 1.2 and 1.8 mA cm^{-2}, respectively (Figure 5c). The much denser structure of GCMP than GCM not only enhances ion conduction but also better barricades Li dendrite propagation under high current densities. Another often neglected issue in NASICON-type SSEs is the thermal runaway of the electrolyte, which might cause safety issues, especially during high-rate operation.[9] In this study, the improvement of SSB thermal stability by GCMP modification is highlighted. As shown in Figure S29 (Supporting Information), the GCMP coating layer accelerates thermal dissipation after laser thermal radiation, which is mainly attributed to the excellent thermal conductivity of the graphene and carbon nanotubes in GCMP.[28]

The process of full-cell fabrication is depicted in Figure S30, (Supporting Information) (see detailed descriptions in the Experimental Section, Supporting Information). After TPS treatment, the integrative sintering of LATP-based SSBs can be achieved. First, Li||GCMP-LATP||LFP batteries are prepared by FS and TPS methods (denoted as LFP-FS and TPS, respectively), respectively.

© 2023 The Authors. Advanced Energy Materials published by Wiley-VCH GmbH

16146840, 2024, 10, Downloaded from https://advanced.onlinelibrary.wiley.com/doi/10.1002/aenm.202303422 by University Town Of Shenzhen, Wiley Online Library on [19/11/2025]. See the Terms and Conditions (https://onlinelibrary.wiley.com/terms-and-conditions) on Wiley Online Library for rules of use; OA articles are governed by the applicable Creative Commons License

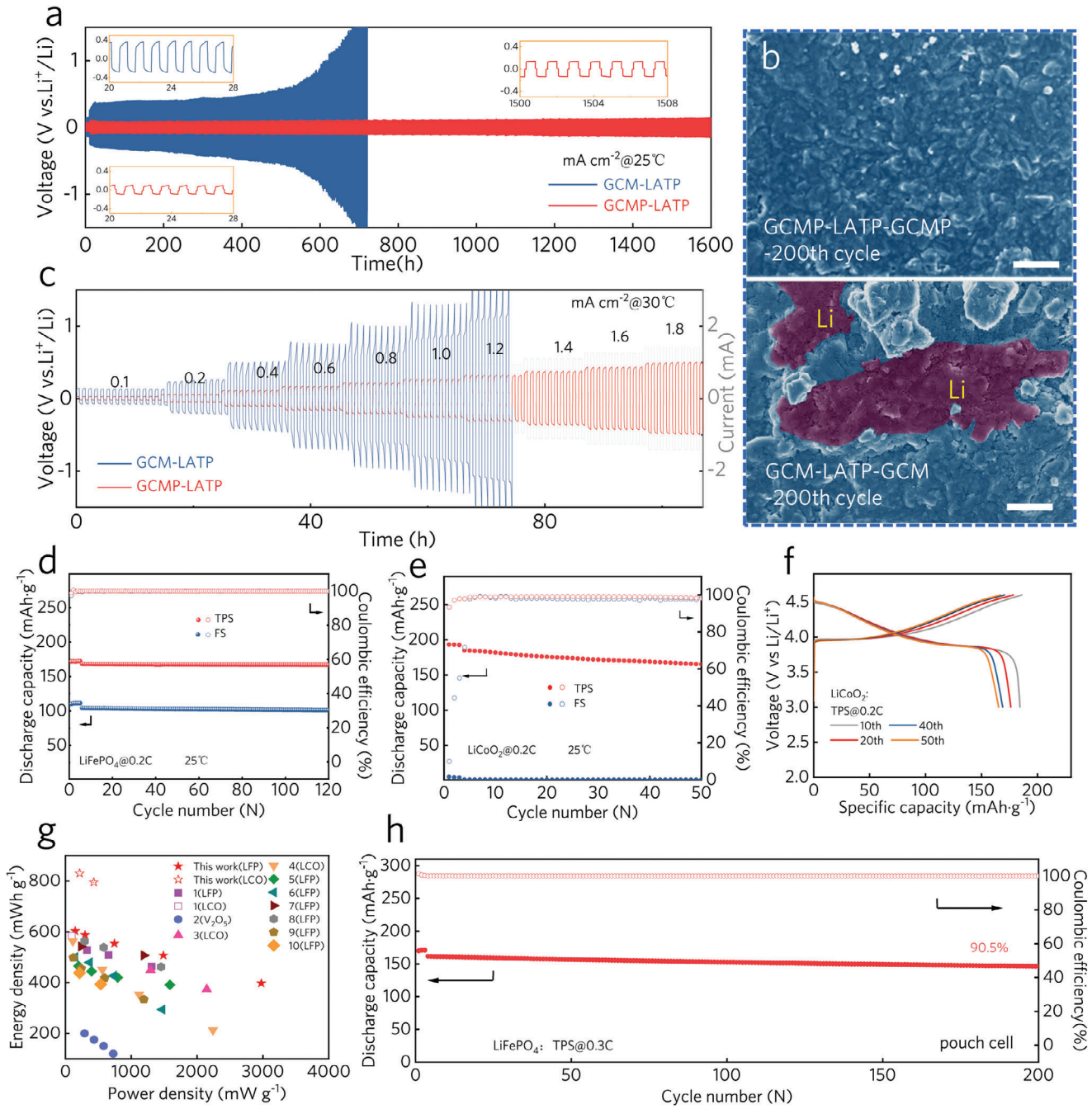

Figure 5. a) Potential profiles of Li-symmetric cells with different electrolytes at a constant current density of 0.2 mA cm−2. Top-viewed SEM images of GCMP-LATP-GCMP b) and GCM-LATP-GCM after the lithium stripping-plating for 200 cycles at 0.2 mA cm−2. c) Voltage profiles in the symmetric cells with different electrolytes at increasing current densities. Cycling performance of LFP (d) and LCO (e) SSBs fabricated by different sintering methods. f) Voltage profiles for the LCO SSB fabricated by the TPS method. g) Comparison of the power density and energy density with previously reported literature (detailed comparisons are listed in Table S1 (Supporting Information). h) Cycling performance of Li/GCMP-LATP/LFP pouch cell.

The cycling performance of SSBs based on the above two different integrated sintering methods is compared in Figure 5d, where LFP-TPS delivered the higher discharge capacity (168 mAh g^{-1}) compared with LFP-FS (104 mAh g^{-1}). Based on EIS results (Figure S31a, Supporting Information), this discrepancy can be attributed to the inhibition effect of TPS on side reactions at grain boundaries. In addition, the extremely high capacity retention (99.1% after 120 cycles) and average coulombic efficiency (99.9%) achieved by LFP-TPS indicate a stable cathode-electrolyte interface during cycling, which was verified by the voltage profiles (Figure S32, Supporting Information) and EIS (Figure S31b, Supporting Information), where no voltage decay or interfacial degradation can be observed after 120 cycles. According to the in situ EIS of the LFP cathode at the 1st cycle, the resistance of the

© 2023 The Authors. Advanced Energy Materials published by Wiley-VCH GmbH

16146840, 2024, 10, Downloaded from https://advanced.onlinelibrary.wiley.com/doi/10.1002/aenm.202303422 by University Town Of Shenzhen, Wiley Online Library on [19/11/2025]. See the Terms and Conditions (https://onlinelibrary.wiley.com/terms-and-conditions) on Wiley Online Library for rules of use; OA articles are governed by the applicable Creative Commons License

cathode-electrolyte interface and Li^+ charge transfer remained unchanged, suggesting a stable interface formed between the cathode and electrolyte through TPS (Figure S33, Supporting Information). At a rate of 0.5 C (1 C = 170 mA g^{-1}), LFP-TPS can function for 500 cycles with high discharge capacity (140 mAh g^{-1}) and a capacity retention of 90.1%, which reveals the superb long-term cyclability (Figure S34, Supporting Information). The rate tests further show that LFP-TPS deliver satisfactory discharge capacities at elevated rates (145 and 114 mAh g^{-1} at 1 C and 2 C respectively (Figure S35, Supporting Information).

Due to the incompatibility of LATP and carbonate electrolyte,[29] it is difficult to realize the high-voltage operation of SSBs by using a catholyte. Herein, full batteries with LCO cathode prepared by FS and TPS (denoted as LCO-FS and LCO-TPS, respectively) were also assembled and tested between 3.0 and 4.6 V (Figure 5e,f). Different from LFP-FS, which still releases capacities over 100 mAh g^{-1}, LCO-FS shows an abysmal initial discharge capacity of merely 5.3 mAh g^{-1} with a coulombic efficiency of ≈10.0%. This result might be attributed to the severe side reaction (i.e., Co diffusion) between LCO and LATP, as previously demonstrated in Figure 4d, hence the catastrophic loss of active LCO. As a clear contrast, LCO-TPS exhibits an initial discharge capacity of 185 mAh g^{-1} with a coulombic efficiency of 98.0% at 0.2 C (1 C = 200 mA g^{-1}). In situ Raman spectra (Figure S36, Supporting Information) show that both characteristic peaks (482 cm^{-1}, E_g and 590 cm^{-1}, A_{1g}) of LCO[30] remain stable during cycling, indicating the well-preserved crystalline structure of LCO. More importantly, this cell shows relatively stable cycling with ≈89% capacity retention after 50 cycles. To analyze the fading mechanism, postmortem SEM images of LCO cathodes after cycling were carried out (Figure S37, Supporting Information), where some LCO particles exhibit evident cracks. Hence, the capacity attenuation might be related to the uneven stress distribution of micro-sized LCO during the cycling on the solid–solid interfaces, leading to the particle crack. Also, the increase of R_{ct} resistance after cycling implies the occurrence of interfacial issues (Figure S38, Supporting Information).

As a comparison, the LFP-SSB prepared by the typical UHS sintering method (≈10s, Figure S39a, Supporting Information) exhibits moderate discharge capacity (128 mAh g^{-1}) after 120 cycles (Figure S39b, Supporting Information) while the LCO cell shows a sharp decline after ten cycles (Figure S39c, Supporting Information). To determine interfacial side reactions induced by UHS, XRD patterns of cathode mixtures (i.e., active materials, LATP, and acetylene black) were also examined (Figure S39d,e, Supporting Information), where more byproducts can be observed compared with TPS. We speculate that compared with the pulsed heating in TPS, the continuous heating in UHS enables longer phase diffusion time, resulting in an inferior mitigating effect on the side reactions between LATP and cathodes, hence the lower initial capacity and faster capacity decline.

The comparison of the power density and energy density delivered by LCO-TPS and LFP-TPS with those previously reported ISE-based solid-state batteries via various sintering methods (Figure 5g; see details listed in Table S1, Supporting Information) demonstrates that this work exhibits a state-of-the-art energy densities and power densities. To further demonstrate the practicability of the TPS method, proof-of-concept LFP-TPS pouch cells were assembled and tested (Figure 5h). Under the condition of 0.3 C, the LFP-TPS pouch cell achieved stable cycling for 200 cycles, manifesting the wide application potential of the TPS method in fabricating ISE-based solid batteries.

3. Conclusion

In summary, a scalable and controllable thermal pulse sintering method to fabricate SSBs is proposed to overcome the interfacial issues between cathode materials, LATP electrolytes, and Li metal. The rapid thermal shock process could improve the density of LATP SSEs by inducing the growth of LATP NWs, which fill up the voids and increase the ionic conductivity. Simultaneously, a compact protective layer (GCMP) was constructed on the anode side, providing additional Li^+ conduction pathways to enable a stable and robust LATP/Li interface. More importantly, the intense yet transient thermal pulse helps fast welding of the surface between the cathode and SSE to promote interfacial contact without causing detrimental side reactions. Benefiting from the proposed sintering strategy, 4.6 V LCO-based SSB can be stably cycled, delivering a high specific capacity of 185 mAh g^{-1}. The assembled LFP-based SSB also delivered a high capacity retention of 90.8% over 500 cycles. The key findings of this work pave the way for the practical application of ISEs in high-voltage SSBs.

Supporting Information

Supporting Information is available from the Wiley Online Library or from the author.

Acknowledgements

X.Y. and S.C. contributed equally to this work. L.Y. acknowledges the support from the Shenzhen Science and Technology Planning Project (JSGG20220831095604008). Y. Song acknowledges the support from the National Natural Science Foundation of China (No. 52102200). X. Sun acknowledges supported by the Natural Sciences and Engineering Research Council of Canada (NSERC); Canada Research Chair Program (CRC); Canada Foundation for Innovation (CFI); Ontario Research Fund (ORF); Interdisciplinary Development Initiatives (IDI) by Western University; and University of Western Ontario. C.W. and X.S. were grateful for the support from the Eastern Institute for Advanced Study (EIAS), Eastern Institute of Technology, Ningbo. The authors thank the Shanghai Synchrotron Radiation Facility (SSRF) (beamline 02B02) for the allocation of synchrotron beam time and the support from the XMCD beamline (BL12B) in the National Synchrotron Radiation Laboratory (NSRL).

Conflict of Interest

The authors declare no conflict of interest.

Data Availability Statement

Research data are not shared.

Keywords

high-energy-density, LATP, solid-state electrolytes, thermal pulse sintering

Received: October 10, 2023
Revised: November 28, 2023
Published online: December 27, 2023

© 2023 The Authors. Advanced Energy Materials published by Wiley-VCH GmbH

16146840, 2024, 10, Downloaded from https://advanced.onlinelibrary.wiley.com/doi/10.1002/aenm.202303422 by University Town Of Shenzhen, Wiley Online Library on [19/11/2025]. See the Terms and Conditions (https://onlinelibrary.wiley.com/terms-and-conditions) on Wiley Online Library for rules of use; OA articles are governed by the applicable Creative Commons License

[1] J. Bae, Y. Li, J. Zhang, X. Zhou, F. Zhao, Y. Shi, J. B. Goodenough, G. Yu, *Angew. Chemie – Int. Ed.* **2018**, *57*, 2096.
[2] B. Xu, X. Li, C. Yang, Y. Li, N. S. Grundish, P.-H. Chien, K. Dong, I. Manke, R. Fang, N. Wu, H. Xu, A. Dolocan, J. B. Goodenough, *J. Am. Chem. Soc.* **2021**, *143*, 6542.
[3] L. Chen, Y. Li, S.-P. Li, L.-Z. Fan, C.-W. Nan, J. B. Goodenough, *Nano Energy* **2018**, *46*, 176.
[4] J. Janek, W. G. Zeier, *Nat. Energy* **2023**, *8*, 230.
[5] W. Xia, Y. Zhao, F. Zhao, K. Adair, R. Zhao, S. Li, R. Zou, Y. Zhao, X. Sun, *Chem. Rev.* **2022**, *122*, 3763.
[6] C. Wang, Q. Sun, Y. Liu, Y. Zhao, X. Li, X. Lin, M. N. Banis, M. Li, W. Li, K. R. Adair, D. Wang, J. Liang, R. Li, L. Zhang, R. Yang, S. Lu, X. Sun, *Nano Energy* **2018**, *48*, 35.
[7] L. Yang, Y. Song, H. Liu, Z. Wang, K. Yang, Q. Zhao, Y. Cui, *Small Methods* **2020**, *4*, 1900751.
[8] H. Kim, C. Im, S. Ryu, Y. J. Gong, J. Cho, S. Pyo, H. Yun, J. Lee, J. Yoo, Y. S. Kim, *Adv. Funct. Mater.* **2022**, *32*, 2107555.
[9] J. Yan, D. Zhu, H. Ye, H. Sun, X. Zhang, J. Yao, J. Chen, B. Guo, S. Ichikawa, D. Gao, L. Zhang, J. Huang, Y. Tang, *ACS Energy Lett.* **2022**, *7*, 3855.
[10] L. Zhu, Y. Wang, Y. Wu, W. Feng, Z. Liu, W. Tang, X. Wang, Y. Xia, *Adv. Funct. Mater.* **2022**, *32*, 2201136.
[11] Z. Chen, G.-T. Kim, J.-K. Kim, M. Zarrabeitia, M. Kuenzel, H.-P. Liang, D. Geiger, U. Kaiser, S. Passerini, *Adv. Energy Mater.* **2021**, *11*, 2101339.
[12] J. Sun, X. Yao, Y. Li, Q. Zhang, C. Hou, Q. Shi, H. Wang, *Adv. Energy Mater.* **2020**, *10*, 2000709.
[13] Z. Cheng, T. Liu, B. Zhao, F. Shen, H. Jin, X. Han, *Energy Storage Mater.* **2021**, *34*, 388.
[14] X. Han, S. Wang, Y. Xu, G. Zhong, Y. Zhou, B. Liu, X. Jiang, X. Wang, Y. Li, Z. Zhang, S. Chen, C. Wang, Y. Yang, W. Zhang, J. Wang, J. Liu, J. Yang, *Energy Environ. Sci.* **2021**, *14*, 5044.
[15] Q. Xu, Z. Liu, A. Windmüller, S. Basak, J. Park, K. Dzieciol, C.-L. Tsai, S. Yu, H. Tempel, H. Kungl, R.-A. Eichel, *Small* **2022**, *18*, 2200266.
[16] S. Chen, L. Nie, X. Hu, Y. Zhang, Y. Zhang, Y. Yu, W. Liu, *Adv. Mater.* **2022**, *34*, 2200430.
[17] T. Pan, W. Zhou, Q. Wei, Z. Peng, H. Wang, X. Jiang, Z. Zang, H. Li, D. Yu, Q. Zhou, M. Pan, W. Zhou, Z. Ning, *Adv. Mater.* **2023**, *35*, 2208522.
[18] Z. Zhao, R. Wang, C. Peng, W. Chen, T. Wu, B. Hu, W. Weng, Y. Yao, J. Zeng, Z. Chen, P. Liu, Y. Liu, G. Li, J. Guo, H. Lu, Z. Guo, *Nat. Commun.* **2021**, *12*, 6606.
[19] J. Lu, S. Liu, J. Liu, G. Qian, D. Wang, X. Gong, Y. Deng, Y. Chen, Z. Wang, *Adv. Energy Mater.* **2021**, *11*, 2102103.
[20] M. Song, Z. Yi, R. Xu, J. Chen, J. Cheng, Z. Wang, Q. Liu, Q. Guo, L. Xie, C. Chen, *Energy Storage Mater.* **2022**, *51*, 620.
[21] S. Chen, Z. Song, L. Wang, H. Chen, S. Zhang, F. Pan, L. Yang, *Acc. Chem. Res.* **2022**, *55*, 2088.
[22] C. Zhu, S. Chen, K. Li, Z.-W. Yin, Y. Xiao, H. Lin, F. Pan, L. Yang, *Sci. Bull.* **2023**, *68*, 408.
[23] L. Dai, J. Wang, Z. Shi, L. Yu, J. Shi, *Ceram. Int.* **2021**, *47*, 11662.
[24] R. Baddour-Hadjean, J.-P. Pereira-Ramos, *Chem. Rev.* **2010**, *110*, 1278.
[25] Q. Gan, N. Qin, Y. Zhu, Z. Huang, F. Zhang, S. Gu, J. Xie, K. Zhang, L. Lu, Z. Lu, *ACS Appl. Mater.* **2019**, *11*, 12594.
[26] Z. Wei, C. Liang, L. Jiang, L. Wang, S. Cheng, Q. Peng, L. Feng, W. Zhang, J. Sun, Q. Wang, *Energy Storage Mater.* **2022**, *47*, 51.
[27] A. Manthiram, J. B. Goodenough, *Nat. Energy* **2021**, *6*, 844.
[28] L. Zhong, L. Guo, J. Wang, Q. Song, H. Li, Y. Li, *Carbon* **2023**, *208*, 123.
[29] J. Zhu, J. Zhao, Y. Xiang, M. Lin, H. Wang, B. Zheng, H. He, Q. Wu, J. Y. Huang, Y. Yang, *Chem. Mater.* **2020**, *32*, 4998.
[30] H. Huang, Z. Li, S. Gu, J. Bian, Y. Li, J. Chen, K. Liao, Q. Gan, Y. Wang, S. Wu, Z. Wang, W. Luo, R. Hao, Z. Wang, G. Wang, Z. Lu, *Adv. Energy Mater.* **2021**, *11*, 2101864.

© 2023 The Authors. Advanced Energy Materials published by Wiley-VCH GmbH

16146840, 2024, 10, Downloaded from https://advanced.onlinelibrary.wiley.com/doi/10.1002/aenm.202303422 by University Town Of Shenzhen, Wiley Online Library on [19/11/2025]. See the Terms and Conditions (https://onlinelibrary.wiley.com/terms-and-conditions) on Wiley Online Library for rules of use; OA articles are governed by the applicable Creative Commons License